9-2013

Allosteric Mechanism of Water Channel Gating by Ca2+–calmodulin

Steve Reichow
reichow@pdx.edu

Daniel M. Clemens
University of California, Irvine

J. Alfredo Freites
University of California, Irvine

Karin L. Németh-Cahalan
University of California, Irvine

Matthias Heyden
University of California, Irvine

See next page for additional authors

Let us know how access to this document benefits you.

Follow this and additional works at: https://pdxscholar.library.pdx.edu/chem_fac

Part of the Biochemistry Commons, and the Structural Biology Commons

Citation Details

Reichow, S. L., Clemens, D. M., Freites, J. A., Németh-Cahalan, K. L., Heyden, M., Tobias, D. J., ... & Gonen, T. (2013). Allosteric mechanism of water-channel gating by Ca2+–calmodulin. Nature structural & molecular biology, 20(9), 1085-1092.

Authors

Steve Reichow, Daniel M. Clemens, J. Alfredo Freites, Karin L. Németh-Cahalan, Matthias Heyden, Douglas J. Tobias, James E. Hall, and Tamir Gonen

Allosteric mechanism of water channel gating by Ca2+–calmodulin

Steve L. Reichow[1,4], **Daniel M. Clemens**[2,4], **J. Alfredo Freites**[3], **Karin L. Németh-Cahalan**[2], **Matthias Heyden**[3], **Douglas J. Tobias**[3], **James E. Hall**[2], and **Tamir Gonen**[1]

[1]Janelia Farm Research Campus, Howard Hughes Medical Institute, Ashburn VA, USA

[2]Department of Physiology and Biophysics, University of California Irvine, Irvine CA, USA

[3]Department of Chemistry, University of California Irvine, Irvine CA, USA

Abstract

Calmodulin (CaM) is a universal regulatory protein that communicates the presence of calcium to its molecular targets and correspondingly modulates their function. This key signaling protein is important for controlling the activity of hundreds of membrane channels and transporters. However, our understanding of the structural mechanisms driving CaM regulation of full-length membrane proteins has remained elusive. In this study, we determined the pseudo-atomic structure of full-length mammalian aquaporin-0 (AQP0, *Bos Taurus*) in complex with CaM using electron microscopy to understand how this signaling protein modulates water channel function. Molecular dynamics and functional mutation studies reveal how CaM binding inhibits AQP0 water permeability by allosterically closing the cytoplasmic gate of AQP0. Our mechanistic model provides new insight, only possible in the context of the fully assembled channel, into how CaM regulates multimeric channels by facilitating cooperativity between adjacent subunits.

Keywords

aquaporin (AQP); gating; calmodulin (CaM); electron microscopy (EM); molecular dynamics (MD); calcium regulation; water channel; membrane protein complex

Correspondence should be addressed to: JEH (jhall@uci.edu) or TG (gonent@janelia.hhmi.org), Tamir Gonen, PhD, Ph 571.209.4261, Fax 571.291.6449, James Hall, PhD, Ph 949.824.5835, Fax 949.824.3143.
[4]These authors contributed equally to this work

Introduction

Calmodulin (CaM) is a Ca^{2+} binding protein that functions as a ubiquitous secondary messenger in several Ca^{2+} signaling pathways to dynamically regulate the function of hundreds of proteins. Many membrane proteins that act as transporters and channels, such as the cardiac and neuronal voltage-gated ion channels[1–4], the RyR family of Ca^{2+}-release channels[5–7], Transient Receptor Potential (TRP) channels[8–10], gap junctions[11–13], and the aquaporin water channels[14,15] are modulated by CaM in response to cytoplasmic Ca^{2+} fluctuations.

CaM is a small (16.7 kDa) bi-lobed protein composed of N- and C-terminal Ca^{2+}-binding domains connected by an internal flexible linker domain[16–19]. The N- and C-terminal lobes undergo structural rearrangements upon binding Ca^{2+} to expose a hydrophobic binding pocket that recognizes target proteins. This conformational change supports CaM's Ca^{2+}-dependent recognition mechanism, and its flexibility allows for binding to a diverse set of substrates. In addition, CaM is able to bind many of its cellular targets in its Ca^{2+}-free (apo) state allowing for a constitutive interaction under low Ca^{2+} conditions. In this way CaM acts as an efficient signal transducer that can rapidly modulate the function of its target proteins with a dynamic response to changes in intracellular Ca^{2+} levels[20,21].

Aquaporins (AQPs) are a family of water channels found in all kingdoms of life that facilitate the flux of water molecules across membranes. Humans differentially express 13 AQP isoforms in a tissue-specific manner, each possessing unique substrate permeability characteristics and each regulated in different way [22]. Structurally, all AQPs are tetramers in which each monomer forms its own pore for water. Each monomer consists of six transmembrane helices that pack against one another as in a barrel forming a hydrophilic pore for water permeation. Each AQP tetramer therefore contains 4 water channels. Specificity for water involves the selectivity filter (constriction site 1 (CSI)) located at the extracellular vestibule. CSI constricts the water pore to a diameter of ~3 Å, which is large enough for water to pass but forms a steric barrier to larger molecules[23]. Further down the pore, roughly at its center, two NPA motifs contribute a pair of asparagine residues to form the proton exclusion site used to prevent the passage of protons[23,24]. The pore then expands to form the cytoplasmic vestibule. While all AQPs share this transmembrane structure and pore architecture, the primary sequences of different AQPs vary greatly in their cytoplasmic N- and C-terminal domains, and these are often crucial for channel regulation.

Aquaporin-0 (AQP0) is a water channel that is exclusively expressed in the mammalian eye lens, and whose permeability is directly modulated by CaM[25,26]. AQP0 serves a dual function in the lens by acting as a water channel[27–30] or an adhesive protein mediating cell-cell adhesive junctions[31–33]. Regulation of water permeability by CaM is achieved through a Ca^{2+}-dependent interaction between Ca^{2+}–CaM and the cytoplasmic C-terminal domain of AQP0[26,34,35]. Typically, Ca^{2+}–CaM recognizes and binds its targets by wrapping around a single amphipathic helix. However, in the case of AQP0, Ca^{2+}–CaM interacts in a non-canonical fashion by simultaneously binding to two AQP0 C-terminal helices, resulting in an overall 2:1 (AQP0:CaM) stoichiometry[35]. The functional consequence of Ca^{2+}–CaM

binding to AQP0 is the inhibition of water permeation[26,35] although the mechanism by which this occurs is poorly understood.

Despite the importance of CaM regulation in membrane protein biology, there are currently no structural models for any full-length membrane protein channel in complex with CaM. Instead, numerous structures of CaM bound to fragments of membrane proteins exist, and these are typically small ~20 residue peptides or domains of the channel in complex with CaM[36–39]. This is because full-length channels are often difficult to work with and their associations with CaM can be transient and mediated by flexible domains refractive to structural analysis. CryoEM reconstructions of the Ryanodine Receptor (RyR) in complex with CaM have been reported previously[40,41], however an absence of high-resolution structural information for the RyR channel has prevented a mechanistic understanding of CaM regulation and no pseudo-atomic model of the complete complex has been obtained. Because of these difficulties and lack of information from numerous systems, it became clear that hybrid techniques are required to yield a structural model of CaM bound to a full-length channel to begin to understand how CaM dynamically modulates channel function.

To gain a mechanistic understanding of how CaM is used to modulate the water permeability of AQP0, we employed electron microscopy, structural modeling, molecular dynamics, and functional mutation studies to develop a pseudo-atomic structure of the full-length AQP0 in complex with CaM. Our structural model allowed us to dissect the mechanism by which CaM dynamically modulates AQP0 water channel permeability, and this, in turn was tested experimentally by mutagenesis experiments and permeability studies. This work provides the first structural model of CaM bound to any full-length channel. Our mechanistic model provides new insights into the role of cooperativity in regulating AQPs, and offers cues into how CaM allosterically modulates the functions of other membrane channels.

Results

Pseudo-atomic model of the AQP0–calmodulin complex

Native AQP0 and recombinant CaM were purified to homogeneity and the complex was formed in the presence of calcium as previously described[35]. The AQP0–CaM complex was stabilized for electron microscopy (EM) studies using the zero-length cross-linking reagent 1-ethyl-3-(3-dimethylaminopropyl) carbodiimide (EDC). The AQP0–CaM cross-linked complex was effectively separated from excess CaM by size-exclusion chromatography (SEC) (Figure 1a – b). The purified complex eluted as a monodispersed species with a retention time consistent with the fully assembled AQP0–CaM complex, consisting of an AQP0 tetramer in a detergent micelle in complex with two CaM molecules (Figure 1a). The peak fraction was assessed by denaturing SDS-PAGE, which identified three species with apparent molecular weights of ~26 kD, ~39 kD, and ~65 kD, corresponding to the AQP0 monomer, the 1:1 AQP0–CaM cross-link and the 2:1 (AQP0)$_2$–CaM cross-link, *respectively* (Figure 1b and Supplementary Figure S1).

The purified AQP0–CaM complex was negatively stained and visualized by EM. The AQP0–CaM complexes appeared as homogeneous particles ~7 nm in size and evenly

distributed on the EM grid (Figure 1c). Projection-averages revealed predominant views consisting of square-shaped structures (Figure 1c) and views that contained distinctive bi-lobed features interpreted as side views (Figure 1c). An initial three-dimensional (3D) reconstruction was calculated from the tilted-pair dataset by random-conical methods[42] and further refined using FREALIGN[43] resulting in a final ~25 Å reconstruction (Figure 1d).

The 3D reconstruction of the AQP0–CaM complex is a bi-lobed structure, consisting of a square-shaped domain with two protrusions extending off the face of the main body. The square shaped domain is 65×65 Å when viewed from the "top" of the reconstruction (Figure 1d). This top view is consistent with the square-shaped views observed in projection-averages (Figure 1c). Rotating the map 90° along the x-axis gives a "side-view" of the reconstruction standing at 75 Å tall and revealing the two lobes extending from the main domain, each 40 Å wide and 35 Å tall (Figure 1d). These features correspond well with the bi-lobed features observed in the projection-averages (Figure 1c). The main square-shaped domain is 40 Å tall when viewed from the side (Figure 1d). An additional 90° rotation along the x-axis displays the "bottom" of the reconstruction showing the two lobes of the EM map oriented toward the reader separated by a cleft ~10–15 Å wide (Figure 1d). In this work, we refer to the "top" and "bottom" as the extracellular and cytoplasmic views, respectively.

The EM map was used to guide the construction of a pseudo-atomic model of AQP0 in complex with CaM (Figure 1e – f and Supplementary Figure S2). The crystal structure of the AQP0 tetramer (PDB 2B6P;[30]) fit well into the main body of the EM map (65×65×40 Å) while CaM fit well into the two lobe features seen in side views of the particles (40×35 Å). The AQP0 tetramer was placed with its cytoplasmic side facing the lobe features of the EM map. This initial fitting was computationally minimized using Chimera[44] (Figure 1e).

We previously demonstrated that CaM binds two cytoplasmic AQP0 C-terminal helices simultaneously[35]. The only conformational arrangement that facilitated this binding mode in the AQP0 tetramer was for two neighboring C-terminal helices to come together in an anti-parallel fashion. Of the more than 200 CaM complexes currently deposited in the Protein Data Bank (www.rcsb.org) there are only two structures of Ca^{2+}–CaM bound to two adjacent antiparallel helices. These belong to plant glutamate decarboxylase (*pt*GAD)–CaM complex[45] and the voltage-gated calcium channel ($Ca_{V1.2}$)–CaM complex[46,47]. Only the compact structure of the *pt*GAD–CaM complex fit well within the 40×35 Å lobes of the EM reconstruction (Figure 1e). The cytoplasmic C-terminal α-helices of AQP0 (residues 227–241) were modeled using the anti-parallel *pt*GAD α-helices as templates and connected to the transmembrane domain of AQP0 by short linker domains (residues 223–226) (**Methods** and Supplementary Figure S2). The resulting pseudo-atomic model of the AQP0–CaM complex contains the two Ca^{2+}–CaM molecules located directly beneath two of the AQP0 subunits and bound to the C-terminal helices of adjacent monomers (Figure 1f). Following energy minimization the final model displayed no steric clashes and a calculated map at 25 Å yielded a cross-correlation of 0.95 compared to the experimental map.

Calmodulin uses a hydrophobic "bind and capture" mechanism

The AQP0 CaM binding domain (AQP0^{CBD}) contains an α-helix with several highly conserved hydrophobic residues that could be recognized by the hydrophobic N- and C-lobe

binding pockets in Ca^{2+}–CaM (Figure 2a). To determine which of these residues are involved in CaM recognition we mutated each individual site to alanine and characterized the thermodynamic effects on binding to CaM using isothermal titration calorimetry (ITC) (Figure 2a – c and Supplementary Figure S3).

ITC studies were performed using 20-residue peptides corresponding to the bovine AQP0^{CBD} sequence shown in Figure 2a. The wildtype AQP0^{CBD} produced large heats of binding when mixed with CaM that fit well to a two-state binding model (Figure 2b). The stepwise binding showed an initial high-affinity event with an association constant (K_{a1} ~ 1.4×10^7 M^{-1}) followed by a second lower-affinity binding event (K_{a2} ~ 7.8×10^4 M^{-1}). Fitting of the energetic parameters to a two-state binding model yielded an overall free energy (G_{1+2}) equal to −16.4 kcal•mole^{-1} (Supplementary Figure S3 contains a full table of thermodynamic parameters obtained by ITC). Each of the AQP0^{CBD} mutations resulted in unique thermodynamic effects on binding to CaM (Figure 2c). Mutating residues L227A and V230A resulted in the largest overall energetic penalties G_{1+2} of 8.4 kcal•mole^{-1} and 7.75 kcal•mole^{-1}, *respectively*. Only a 1:1 stoichiometric complex was formed with CaM using these two mutant peptides, in contrast to the 2:1 stoichiometry displayed by the wildtype AQP0^{CBD} (Figure 2c). Mutation of hydrophobic residues L234A and L237A also showed reduced binding affinity compared to wildtype, but these mutants could maintain a 2:1 complex with CaM. The L234A mutation resulted in an ~83% reduction in K_{a1} and a 38% reduction in K_{a2} (Figure 2c), with an overall G_{1+2} of 1.3 kcal•mole^{-1}. The L237A mutation showed a 63% reduction in K_{a1}, while K_{a2} was essentially unaffected (Figure 2c), resulting in an overall G_{1+2} of 0.5 kcal•mole^{-1}. Uniquely, mutating I236 to alanine produced an enhanced binding energy G_{1+2} of −0.87 kcal•mole^{-1}. This enhanced affinity is primarily due to a more favorable interaction during the second binding event (K_{a2}) that was increased ~410% over wildtype (Figure 2c).

To assess the structural context of these mutational effects, the AQP0^{CBD} residues were mapped to a two-dimensional helical wheel representation (Figure 2d). Notably, the hydrophobic residues that resulted in energetic penalties upon mutation to alanine (L227, V230, L234 and L237) all cluster along the same face of the AQP0^{CBD} α-helix. In contrast, the residue I236 that resulted in an enhanced binding affinity when mutated to alanine is located on the opposing side of the α-helix, which is characterized by a mixture of hydrophilic residues (Figure 2d). This analysis suggests that it is this hydrophobic face of the AQP0^{CBD} that interacts with the N- and C-lobe binding pockets of CaM during complex formation. In our structure of the AQP0–CaM complex the AQP0^{CBD} domains are modeled with the hydrophobic faces displayed toward the N- or C-lobe binding pockets of CaM (Figure 2e), while the hydrophilic face is primarily solvent exposed.

In the CaM–free AQP0 crystal structure the C-terminal α-helices of AQP0 are positioned beneath each monomer and stabilized in this orientation, in part, by van der Waals interactions formed between the hydrophobic AQP0^{CBD} residue L237 and the cytoplasmic loop residue L83 (ref. 30). For CaM to bind AQP0 this interaction must be broken to allow the C-termini of neighboring monomers to rotate and come together to form the anti-parallel configuration that is stabilized by CaM. Our binding studies suggest this configuration is stabilized by CaM through a step-wise "bind and capture" mechanism driven by

hydrophobic interactions. The initial high-affinity 1:1 binding interaction would allow CaM to bind the AQP0 tetramer in the absence of a preformed anti-parallel configuration between neighboring AQP0[CBD] domains (Figure 2f). Once a 1:1 complex is formed, the close proximity of a neighboring AQP0[CBD] domain would allow CaM to readily capture a second AQP0[CBD] in the anti-parallel arrangement (Figure 2f). The mutations studied here revealed distinct energetic contributions for each binding event, suggesting these hydrophobic sites participate in separate and unique roles during this two-step "bind and capture" mechanism for forming the AQP0–CaM complex.

Calmodulin stabilizes AQP0, and closes the channel gate

There are several mechanisms by which CaM binding to the AQP0 C-terminus could inhibit water channel permeability. In our structural model of the AQP0–CaM complex the two CaM molecules are positioned directly below the cytoplasmic pores of two of the four AQP0 monomers (Figure 1f and Figure 2f). This arrangement suggested that CaM could potentially act as a plug[35]. However, 3D water density and pore profile analysis using the program HOLE[48] show the cytoplasmic vestibule of these subunits could remain open and accessible to bulk water even when in complex with CaM (Figure 3a – b). Therefore, to get insight into the change in the channel conformational dynamics that occur when CaM is bound we conducted a comparative molecular dynamics (MD) study on the CaM–free and CaM–bound AQP0 tetramer. The starting points of the two simulations contained identical conformations of the AQP0 tetramer in a POPC lipid-bilayer with or without the two CaM molecules (Supplementary Figure S4). After equilibration of the two systems, the two MD simulations ran for ~500 ns.

The calculated single channel water permeability (p_f) for the CaM–free AQP0 tetramer was 2.1×10^{-15} ($\pm 1.8 \times 10^{-15}$) $cm^3 \cdot s^{-1}$ (ref. 49), consistent with previous MD and functional studies[28,50–52]. In the CaM–bound AQP0 simulation p_f values within the tetramer were reduced, to as low as 0.035×10^{-15} $cm^3 \cdot s^{-1}$. These results are in line with our previous functional studies showing CaM binding to AQP0 results in water channel inhibition[14,26]. To gain further insight into the mechanism of water channel inhibition the conformational dynamics of AQP0 were assessed by the per-residue α-carbon root-mean-squared fluctuations (RMSF) (Figures 3c – e). RMSF clustering analysis shows CaM binding limits the overall dynamics of each of the AQP0 monomers in the tetramer. The highest RMSF values in the CaM–free system mapped to the extracellular loops and the cytoplasmic C-terminus, the site of CaM binding (Figure 3c – d), while residues within the transmembrane domain exhibited low thermal fluctuations (Figure 3c – d). This result is in agreement with the experimental temperature factors obtained by electron crystallography of AQP0 in a lipid membrane[30].

Unlike most other aquaporins, the channel pore of AQP0 contains a second constriction site termed CSII that is located at the cytoplasmic vestibule of the channel[33]. Residues forming CSII were among the most dynamic during the CaM–free MD simulation (Figure 3d). In the CaM–bound simulation, the dynamics of the AQP0 C-terminal α-helices were markedly reduced when confined by CaM (Figure 3e). In addition, the most stabilized residues were mapped to the base of the last transmembrane helix (TM-6) and residues composing the

CSII (Figure 3e). These results indicate that CaM constrains the dynamics of AQP0, particularly by stabilizing the CSII region.

Stabilization of the AQP0 CSII in the CaM–bound MD simulation was intriguing because this site has been proposed to act as a dynamic channel gate[33,50]. The conserved residues Phe75, His66, and Tyr149 form CSII in AQP0 (Figure 4a – b). Tyr149 displayed large movements during the time-course of the simulations. The side chain conformation oscillated between a downward "open" orientation (Figure 4b) and an upward "closed" orientation (Figure 4b and Supplementary Video 1). The difference in pore diameter between the "open" and "closed" states was ~2.5 Å, while in the closed orientation Tyr149 narrows the pore diameter at CSII to ~1.5 Å (Figure 4c). This tight closure would effectively block the passage of water molecules.

To assess the differences in the dynamics at CSII for the AQP0–CaM complex, we monitored the distance between Tyr149 and the opposed residue Phe75 over the time-course of the two simulations (Figure 4d). In the CaM–free system, the distance between these residues varied between ~3.5–12 Å with a main distribution centered at 6.6 Å, and a second smaller population centered at 9 Å (Figure 4d). In the CaM–bound system, the distance between the residues shifted more toward pore closure (Figure 4d). The CaM–bound system also exhibited a major population centered at 6.4 Å, but in addition, a new population of structures with shorter inter-residue displacement was observed (Figure 4d). Furthermore, the population of structures centered at the large 9 Å displacement in the CaM–free system were essentially absent in the CaM–bound system. This analysis indicated that the probability of CSII adopting a closed state increases in the presence of CaM.

Mutation of the AQP0 gate abolishes Ca^{2+}–CaM regulation

Our MD results indicated Ca^{2+}–CaM binding to the AQP0 C-terminus causes a shift in the equilibrium between the "open" and "closed" states of the channel. This result suggested an intimate relationship between CaM binding to the C-terminus of AQP0 and the conformational dynamics of the conserved residues forming the CSII gate. If this relationship is indeed present, mutating the CSII residues should abrogate Ca^{2+}–CaM regulation of water channel permeability. To test this hypothesis we assayed bulk water channel permeability rates of wildtype AQP0 and various AQP0 CSII point mutants by monitoring cell swelling of *Xenopus laevis* oocytes under varying calcium concentrations.

When calcium was removed from the buffer (0 mM Ca^{2+} with 2mM EGTA), Oocytes expressing wildtype AQP0 exhibited bulk water permeability rates (P_f) of $44.6 \times 10^{-5} \pm 2.8 \times 10^{-5}$ μm•s^{-1} well above control cells (Figure 4e). In the presence of high calcium (1.8 mM Ca^{2+}) the rate of water channel permeability was approximately halved ($P_f = 20.2 \times 10^{-5} \pm 5.2 \times 10^{-5}$ μm•s^{-1}, $P_{value} = 0.012$) consistent with previous experimental results[14,26].

Our MD studies suggested Tyr149 acts as the dynamic gating residue at CSII. When this residue was mutated either to a glycine, leucine, or serine the channels maintained their ability to facilitate water flux, however they lost the ability to respond to high calcium conditions. In the Y149G mutant, channels displayed increased water permeability rates (at low calcium) compared to wildtype channels ($P_f = 50.6 \times 10^{-5} \pm 0.5 \times 10^{-5}$ μm•s^{-1}) and

resulted in a complete loss of response to high calcium (Figure 4e). This result suggested that a drastic reduction of the side chain size at this position of the CSII essentially removes the gate altogether and eliminates calcium sensitivity. When Tyr149 is mutated to leucine (Y149L) the channels displayed only low permeabilities that were also unaffected by calcium ($P_f = 19.2 \times 10^{-5} \pm 1.2 \times 10^{-5}$ μm•s^{-1} under low Ca^{2+} and $17.2 \times 10^{-5} \pm 0.8 \times 10^{-5}$ μm•s^{-1} under high Ca^{2+}) (Figure 4e), suggesting that substitution with a large hydrophobic side chain restricts channel gating and consequently abolishes Ca^{2+}–CaM modulation. Lastly, we mutated Tyr149 to serine (Y149S) because we hypothesized that the hydroxyl group it has in common with tyrosine might be important for the gating mechanism. The Y149S mutant resulted in water permeability rates that were comparable to wildtype channels under low calcium conditions ($P_f = 35.7 \times 10^{-5} \pm 6.1 \times 10^{-5}$ μm•s^{-1}), and displayed marginal reduction (~30%) in permeability rates under high calcium ($P_f = 24.4 \times 10^{-5} \pm 5.3 \times 10^{-5}$ μm•s^{-1}) (Figure 4e) suggesting that serine can partially mimic the gating mechanism mediated by Tyr149.

These experimental data are consistent with our MD-based results suggesting that the AQP0 CSII residue Tyr149 alters both the magnitude of the water permeability and its calcium modulation. The data also demonstrates that Tyr149 serves as a dynamic channel gate that allosterically couples Ca^{2+}–CaM binding at the AQP0 C-terminus to water channel closure at CSII.

Discussion

Calmodulin regulates the activity of numerous membrane channels in response to changes in intracellular Ca^{2+} concentration. Despite this central role in channel regulation, very little is known about the underlying structural and molecular mechanisms by which CaM modulates channel function. In this study we used hybrid methods to determine the pseudo-atomic structure of the AQP0 water channel in complex with CaM, providing the first complete structural model for any full-length membrane channel in complex with CaM.

The resulting AQP0–CaM structure shows the AQP0 tetramer in complex with two CaM molecules. We were able to obtain mechanistic insight into CaM regulation using MD simulations, which showed CaM binding to the AQP0 C-terminus allosterically modulates the dynamics at the CSII pore constriction site, resulting in channel closure. The bridging of CaM across two neighboring subunits of AQP0 provides a mechanical force, or tension, that acts on the dynamics of the AQP0 CSII. Our MD analysis shows the stabilizing effect of CaM binding at the AQP0 C-terminus is propagated over ~15 – 20 Å to the CSII site through the cytoplasmic linker and the last transmembrane helix (TM6) of each channel (Figure 3). This allosteric mechanism was experimentally supported by mutagenesis and functional studies that showed CaM regulation of AQP0 water permeability is effectively blocked when the CSII gating residue Tyr149 is mutated. Together, our results show that CaM binding at the AQP0 C-terminus is communicated to the CSII gate via allosteric interactions that favor a closed conformation, thereby dynamically modulating water permeability in a Ca^{2+} dependent manner (Figure 5).

We demonstrated that CaM binds full length AQP0 with a 2:1 (AQP0:CaM) stoichiometry using chemical crosslinking, structural EM analysis and ITC binding studies (Figure 1 and Figure 2), confirming previous studies using NMR spectroscopy[35]. In the AQP0 structure, the only way to facilitate this type of interaction is for two α-helical CaM binding domains from neighboring subunits to come together in an anti-parallel orientation[35]. Based on these results, we have proposed a step-wise "bind and capture" mechanism used by CaM to assemble the 2:1 AQP0-CaM complex (Figure 2f). There are currently only two high-resolution structures of CaM bridging two α-helical peptides, belonging to the *pt*GAD–CaM complex[45] and the $Ca_{V1.2}$–CaM complex[46,47]. In either case, the CaM binding domains adopt anti-parallel α-helical orientations that intersect similar to other dimeric coiled-coil interactions. In the *pt*GAD–CaM complex, a single CaM wraps around the intersection of the *pt*GAD dimer in a compact conformation. Unlike the step-wise association with AQP0, CaM appears to bind both *pt*GAD α-helices simultaneously[53]. In the $Ca_{V1.2}$–CaM complex, two CaM molecules bind to a $Ca_{V1.2}$ helical dimer with each CaM adopting an extended conformation that bridges the $Ca_{V1.2}$ dimer distant from the helical intersection. Our EM data suggested the interaction of AQP0 with CaM was most consistent with that of the compact *pt*GAD–CaM complex. While our structural studies suggest the AQP0–CaM interaction is similar to the *pt*GAD–CaM interaction, the regulatory mechanisms are quite different. For *pt*GAD, CaM binding relieves an auto-inhibitory domain of the enzyme that results in functional activation[54]. For AQP0, CaM binding induces allosteric changes in the channel gate that restrict water permeation. In both cases, a 2:1 stoichiometry may provide a more economical use of CaM. However, for AQP0 this stoichiometry is thought to have an important functional role in the regulatory mechanism.

CaM binding to two neighboring AQP0 C-terminal domains stabilizes the cytoplasmic region of the channel, including the CSII gate. The AQP0 C-termini can be thought of as the reins of the channel through which Ca^{2+}–CaM provides the mechanical force to restrain the channel gate and stabilize the channel in its closed state (Figure 5). This may be similar to the mechanisms used to regulate other channels whose gating properties are modulated by CaM, such as the small conductance potassium (SK) channel[55]. Crystallographic studies of the C-terminal domain from the SK channel bound to CaM in the presence or absence of Ca^{2+} revealed conformational changes that were proposed to drive the activation of the SK channel in a Ca^{2+}-dependent manner[36,56]. Ca^{2+}-free CaM is constitutively associated with a C-terminal domain of SK channels in a 1:1 stoichiometry. When CaM binds Ca^{2+} it associates with an additional SK channel domain from a neighboring subunit to form a 2:2 complex, resulting in a unique structure with CaM extended across three α-helices[36]. This Ca^{2+}-induced interaction was proposed to rotate the C-terminal domain of the SK channel and provide the mechanical force required to open the channel gate[36,56]. Many other channels may utilize similar CaM driven cooperativity to regulate their functions. The NR1 subunits of the NMDA receptor bind CaM with a 2:1 stoichiometry, resulting in channel inactivation[57]. While there is currently no structural information on this complex, it is conceivable that this is another case where the stoichiometry provides the mechanical force used to allosterically drive channel closure.

Unlike other multimeric channels, such as ion channels, cooperativity between AQP subunits is not a functional requirement since each monomer forms its own fully active water pore[58]. Our studies suggest that AQP0 tetramerization is a prerequisite for the binding of regulatory proteins such as Ca^{2+}–CaM. Thus, AQP0 tetramerization appears to provide the necessary scaffold that facilitates cooperative regulatory interactions between subunits. Facilitating cooperativity between neighboring subunits may prove to be a common theme used by CaM to modulate the functions of membrane channels. This possibility emphasizes the need to structurally and mechanistically characterize these interactions using full-length channels. Future studies using complementary structural biology techniques, such as those applied here, will undoubtedly unveil new and unexpected mechanisms used by CaM to regulate its many membrane channel targets.

Online Methods

Crosslinking and purification of the AQP0–CaM complex

The native full-length aquaporin-0 (AQP0) was purified from young sheep lenses and the vertebrate calmodulin (CaM) was heterologously expressed in *E. coli* and purified as previously described[35]. CaM was prepared at 8 mg•ml^{-1} in activation buffer containing 25 mM MES (pH–6.0) and 5 mM $CaCl_2$. The activation reaction was performed with 10 mM 1-ethyl-3-(3-dimethylaminopropyl) carbodimide (EDC, Pierce) and 20 mM N-hydroxysulfosuccinimide (sulfo-NHS, Pierce). The activation reaction was allowed to proceed at room temperature for 15 minutes and unreacted EDC was quenched with 20 mM β-mercaptoethanol (βMe). Activated CaM (2 mg•ml^{-1}) was added to freshly purified AQP0 (1.5 mg•ml^{-1}) (corresponding to a 2 times molar excess of CaM) in crosslinking buffer containing 25 mM HEPES (pH–7.4), 5 mM $CaCl_2$, 5 mM βMe, 0.3% decylmaltoside (DM). The crosslinking reaction was allowed to proceed for 90 minutes at room temperature and quenched by the addition of 10 mM hydroxylamine (Sigma) and placed on ice. The reaction mixture was loaded onto an anion exchange column (capto-adhere, GE Lifescience) equilibrated with 20 mM HEPES (pH–5.5), 1 mM $CaCl_2$ and 0.3% DM. Unreacted AQP0 was separated from the AQP0–CaM cross-linked product by applying a gradient of 750 mM NaCl. The eluted AQP0–CaM cross-linked complex was further purified from excess CaM by size-exclusion chromatography (S200, GE Lifescience) pre-equilibrated with buffer containing 25 mM HEPES (pH–7.4), 5 mM $CaCl_2$ and 0.3% DM. SDS-PAGE and silver staining was used to monitor each step of the purification (Supplementary Figure S1). The absence of a 2:2 AQP0–CaM cross-linked complex or other higher molecular weight aggregates observed by SDS-PAGE demonstrate that the 2:1 stoichiometric complex of AQP0–CaM was specifically stabilized by the EDC reaction. Protein concentrations were determined by BCA assay (Pierce) or UV absorbance at 280 nm.

Electron microscopy and three-dimensional (3D) reconstruction

The freshly purified AQP0–CaM complex was diluted to 0.02 mg•ml^{-1} with buffer containing 25 mM HEPES (pH–7.4), 5 mM $CaCl_2$ and 0.3% DM. 2 μl was applied to a 400 mesh carbon coated EM grid (Ted Pella), stained with uranyl formate (0.75% w/v), blotted on filter paper and dried by laminar air flow. Negatively stained particles were visualized on a 120 kV TEM (FEI) and images were recorded at a nominal magnification of 52,000× at

the specimen level on film (Kodak SO-163) as tilted-pair images (α = 0° and 50°). Images were digitized using a Nikon Coolscan 9000 with a 6.9 μm step size, and binned three times to yield a final pixel size of 3.98 Å per pixel. Thon rings in the power spectra were used to select only those micrographs free of drift or noticeable astigmatism. The contrast transfer function (CTF) parameters were determined for each micrograph using the program CTFTILT[59]. 11,720 particles were selected and processed in SPIDER[42] for generating multivariate reference free projection averages and initial three-dimensional (3D) reconstruction using random conical tilt methods. Final refinement of the 3D density map was performed using FREALIGN[43]. The final 3D density map was reconstructed with C2 symmetry and filtered to 25 Å resolution as suggested by Fourier shell correlation (FSC) analysis.

Molecular modeling of the AQP0–CaM complex

A pseudo-atomic model of the AQP0–CaM complex was built by initially docking available crystal structures into the AQP0–CaM EM density map as follows and in Supplementary Figure S2. The transmembrane domain of the bovine AQP0 crystal structure (PDB 2B6P, residues 9–222)[30] was manually placed into the 65×65×40 Å region of the EM map with the cytoplasmic face of the AQP0 tetramer facing the two vacant lobe domains of the EM map. This initial placement was rotationally and translationally optimized by computational minimization routines in Chimera[44]. The structure of Ca^{2+}–CaM bound to the plant glutamate decarboxylase peptides (ptGAD–CaM, PDB 1NWD)[45] was manually placed within the two vacant lobes of the EM map in a symmetric fashion with the CaM binding clefts facing the AQP0 tetramer. The structure of CaM bound to the voltage-gated calcium channel ($Ca_{V1.2}$)–CaM complex[46,47] was also assessed for fitting into the EM map, however CaM adopts an extended conformation in the $Ca_{V1.2}$–CaM complex that was inconsistent with the dimensions of our EM reconstruction. The helical axis of the two ptGAD subunits were oriented toward the cytoplasmic ends of the last transmembrane helix of neighboring AQP0 monomers. This placement was optimized to avoid steric clashes with AQP0. The two ptGAD α-helical subunits were used as templates to model the AQP0 C-terminal helices from each subunit (residues 227–241). The C-terminal AQP0 α-helical residues L234 and L237 were structurally aligned with the ptGAD hydrophobic anchoring residues Trp485 and Ile482, respectively. The cytoplasmic linkers connecting the AQP0 C-terminal helices to the last transmembrane helix of each subunit (residues 223–226) were manually built and minimized using COOT[60]. The CaM molecules and the AQP0 C-terminal linker and CaM binding domains (residues 223–241) were subjected to steepest decent minimization followed by conjugate gradient minimization routines in Chimera to regularize the geometries and remove steric interactions. A map calculated at 25 Å (σ = 3.5) corresponding to the final model gave a cross-correlation of 0.95 compared to the experimental map (σ = 4.96) in Chimera.

Isothermal titration calorimetry

ITC experiments were performed on a MicroCal VP-ITC (GE Lifescience). $AQP0^{CBD}$ peptides corresponding to the wildtype bovine sequence (residues 223–242), the point mutants L227A, V230A, L234A, I236A, and L237A were synthesized and purified to >98% purity (Biomatik). The $AQP0^{CBD}$ peptides and CaM were dialyzed against 20mM HEPES

(pH–7.0) and 5mM $CaCl_2$ over 72 hours using a 1,000 Da molecular weight cutoff (MWCO) membrane (Spectra•Por). $AQP0^{CBD}$ peptide concentrations were adjusted to 500 μM and titrated into the MicroCal cell containing Ca^{2+}–CaM at 20 μM or dialysis buffer only held at 25° C. ITC data was processed in Origin (OriginLab, Northampton MA) by subtracting the background heats of peptide mixing to buffer alone from heats obtained from mixing with Ca^{2+}–CaM and thermodynamic parameters were obtained by fitting the data to a two-state binding isotherm.

Molecular dynamics simulations

Two simulation systems were generated for POPC embedded AQP0: one for AQP0 in complex with CaM and one for AQP0 alone (CaM–free). The AQP0–CaM complex system was constructed similarly to the structure presented in Figure 1, using PDB 2B6P for AQP0 (residues 5 to 239) and 1NWD for CaM. The complex in our simulations consisted of one AQP0 tetramer, two CaM molecules, 8 Ca^{2+} ions, 410 POPC molecules, and 56,701 waters for a total of 244,011 atoms. For the CaM–free system, a starting conformation of the AQP0 tetramer (residues 5 to 239) in the absence of CaM was created by deleting the CaM coordinates from the AQP0–CaM complex. In this way, the starting conformations of AQP0 in the two simulations were identical. In both systems, the CSII sites of AQP0 were unaltered from the original 2B6P model (Supplementary Figure S4). The simulation for the CaM–free system included the AQP0 tetramer, 410 POPC molecules, 40,175 waters, and 32 counter-ions for a total of 189,933 atoms. These starting configurations were minimized using 1000 steps of conjugate-gradient energy minimization followed by 4 ns of simulation at constant temperature (300 K) and volume with the protein backbone atoms held fixed. The protein backbone atoms were then released in a stepwise manner over 4ns. Unrestrained simulations were run at constant temperature and pressure (1 atm) for 560 ns for the AQP0–CaM complex and 495 ns for the apo–AQP0 system.

The simulations were performed with the NAMD 2.7b1 software package[61]. The CHARMM22 and CHARMM32 force fields[62,63] were used for protein and lipids, respectively, and the TIP3P model was used for water[64]. The smooth particle mesh Ewald method[65] was used to calculate electrostatic interactions. Short-range real-space interactions were cut off at 12 Å, employing a switching function. A reversible multiple time-step algorithm[66] was employed to integrate the equations of motion with a time step of 4 fs for electrostatic forces, 2 fs for short-range non-bonded forces, and 1 fs for bonded forces. All bond lengths involving hydrogen atoms were held fixed. A Langevin dynamics scheme was used for temperature control and a Noseé–Hoover–Langevin piston was used for pressure control[67,68]. Molecular graphics and trajectory analyses were performed using VMD 1.8.7[69] over the last 519 ns (AQP0–CaM system) or 474 ns (CaM–free system) of each trajectory. Water permeabilities were calculated using the method described in Jensen and Mouritsen[49] and implemented in VMD using tcl. In brief, the pore was defined and waters within the pore selected, the velocities of these waters were calculated while they remained in the pore, and the process repeated over the equilibrated portion of the trajectories. The resultant collective coordinate for each trajectory was converted to a collective diffusion constant, which was then converted the single-channel osmotic permeability constant. Statistics,

where shown, were calculated as the average +/– SEM of the four pores from each trajectory. Pore profile analysis was performed using the program HOLE[48].

Water permeability assays

Oocytes from *Xenopus laevis* were obtained from Ecocyte (http://ecocyte-us.com) and injected with 10ng of RNA encoding wild type, Y149G, Y149L, or Y149S AQP0 generated using the mMessage mMachine T3 kit (Ambion/Life Technologies) as described previously[14,26]. Water permeability was calculated from the rate of volume increase which was estimated from automated measurements of the increase in cross-sectional area of the oocyte in response to a dilution of ND96. Swelling rates due to water flow were estimated from measurements of the cross-sectional area of the osmotically challenged oocytes as a function of time. The cross sectional area was measured as a function of time to acquire images of the oocyte at appropriate time intervals (on the order of a few seconds). The number of pixels in the oocyte cross section was calculated automatically by ImageJ and transferred to an Excel spread sheet where pixel number was converted to area using the scale factors of the microscope measured from a stage micrometer. These cross sectional data were used to calculate volume as the 3/2 power of area. From these estimates of volume as a function of time we calculated permeability, an intrinsic property of the membrane, from the formula $P_f = [d(V/V_o)/dt][V_o/S_o]/[{}_{osm}V_w]$. V is the volume as a function of time, V_o is the volume at time 0, S_o is the estimated geometric surface area of the oocyte at time 0, ${}_{osm}$ is the osmotic gradient, V_w is the partial molar volume of water. The initial slope of the $V_{(t)}$ curve was used to determine the value of $d(V/V_o)/dt$ in the formula above. Thus P_f is directly proportional to the observed initial swelling rate. Total membrane expression levels were assayed by Western blot after isolating plasma membrane proteins using the ProteoExtract Native Membrane Protein Extraction Kit (Calbiochem/EMD Millipore). Each sample (corresponding to ~1/2 an oocyte) was separated on a NuPAGE 4–12% Bis-Tris gel (Life Technologies) and transferred to PVDF (Life Technologies) for 1hr at 100V. Levels of AQP0 abundance was probed using an AQP0 primary antibody (1:500 Santa Cruz Biotech AQP0 (H-44) rabbit polyclonal IgG: sc-99059) followed by a secondary antibody (1:10,000 Promega anti-Rabbit IgG HRP) and detection using a Super Signal West Femto kit (Thermo) and exposed on a Fuji LAS-4000 gel documentation system. We note that the accurate assessments of protein abundance from immuno-blots can be problematic.

Supplementary Material

Refer to Web version on PubMed Central for supplementary material.

Acknowledgements

References

1. Saimi Y, Ling KY. Calmodulin activation of calcium-dependent sodium channels in excised membrane patches of Paramecium. Science. 1990; 249:1441–1444. [PubMed: 2169650]

2. Zuhlke RD, Pitt GS, Deisseroth K, Tsien RW, Reuter H. Calmodulin supports both inactivation and facilitation of L-type calcium channels. Nature. 1999; 399:159–162. [PubMed: 10335846]

3. Tan HL, et al. A calcium sensor in the sodium channel modulates cardiac excitability. Nature. 2002; 415:442–447. [PubMed: 11807557]

4. Saimi Y, Kung C. Calmodulin as an ion channel subunit. Annu Rev Physiol. 2002; 64:289–311. [PubMed: 11826271]

5. Meissner G. Evidence of a role for calmodulin in the regulation of calcium release from skeletal muscle sarcoplasmic reticulum. Biochemistry. 1986; 25:244–251. [PubMed: 3754148]

6. Smith JS, Rousseau E, Meissner G. Calmodulin modulation of single sarcoplasmic reticulum Ca2+-release channels from cardiac and skeletal muscle. Circ Res. 1989; 64:352–359. [PubMed: 2536303]

7. Zalk R, Lehnart SE, Marks AR. Modulation of the ryanodine receptor and intracellular calcium. Annu Rev Biochem. 2007; 76:367–385. [PubMed: 17506640]

8. Scott K, Sun Y, Beckingham K, Zuker CS. Calmodulin regulation of Drosophila light-activated channels and receptor function mediates termination of the light response in vivo. Cell. 1997; 91:375–383. [PubMed: 9363946]

9. Zhang Z, et al. Activation of Trp3 by inositol 1,4,5-trisphosphate receptors through displacement of inhibitory calmodulin from a common binding domain. Proc Natl Acad Sci U S A. 2001; 98

10. Zhu MX. Multiple roles of calmodulin and other Ca(2+)-binding proteins in the functional regulation of TRP channels. Pflugers Arch. 2005; 451:105–115. [PubMed: 15924238]

11. Peracchia C, Sotkis A, Wang XG, Peracchia LL, Persechini A. Calmodulin directly gates gap junction channels. J Biol Chem. 2000; 275

12. Sotkis A, et al. Calmodulin colocalizes with connexins and plays a direct role in gap junction channel gating. Cell Commun Adhes. 2001; 8:277–281. [PubMed: 12064602]

13. Peracchia C. Chemical gating of gap junction channels; roles of calcium, pH and calmodulin. Biochim Biophys Acta. 2004; 1662:61–80. [PubMed: 15033579]

14. Nemeth-Cahalan KL, Hall JE. pH and calcium regulate the water permeability of aquaporin 0. J Biol Chem. 2000; 275:6777–6782. [PubMed: 10702234]

15. Varadaraj K, Kumari S, Shiels A, Mathias RT. Regulation of aquaporin water permeability in the lens. Invest Ophthalmol Vis Sci. 2005; 46

16. Babu YS, et al. Three-dimensional structure of calmodulin. Nature. 1985; 315:37–40. [PubMed: 3990807]

17. Zhang M, Tanaka T, Ikura M. Calcium-induced conformational transition revealed by the solution structure of apo calmodulin. Nat Struct Biol. 1995; 2:758–767. [PubMed: 7552747]

18. Kuboniwa H, et al. Solution structure of calcium-free calmodulin. Nat Struct Biol. 1995; 2:768–776. [PubMed: 7552748]

19. Chou JJ, Li S, Klee CB, Bax A. Solution structure of Ca(2+)-calmodulin reveals flexible hand-like properties of its domains. Nat Struct Biol. 2001; 8:990–997. [PubMed: 11685248]

20. Vogel HJ. The Merck Frosst Award Lecture 1994 Calmodulin: a versatile calcium mediator protein. Biochem Cell Biol. 1994; 72:357–376. [PubMed: 7605608]

21. Yamniuk AP, Vogel HJ. Calmodulin's flexibility allows for promiscuity in its interactions with target proteins and peptides. Mol Biotechnol. 2004; 27:33–57. [PubMed: 15122046]

22. Gonen T, Walz T. The structure of aquaporins. Q Rev Biophys. 2006; 39:361–396. [PubMed: 17156589]

23. Murata K, et al. Structural determinants of water permeation through aquaporin-1. Nature. 2000; 407:599–605. [PubMed: 11034202]

24. de Groot BL, Frigato T, Helms V, Grubmuller H. The mechanism of proton exclusion in the aquaporin-1 water channel. J Mol Biol. 2003; 333:279–293. [PubMed: 14529616]

25. Bloemendal H, Zweers A, Vermorken F, Dunia I, Benedetti EL. The plasma membranes of eye lens fibres Biochemical and structural characterization. Cell Differ. 1972; 1:91–106. [PubMed: 4275925]

26. Nemeth-Cahalan KL, Kalman K, Hall JE. Molecular basis of pH and Ca2+ regulation of aquaporin water permeability. J Gen Physiol. 2004; 123:573–580. [PubMed: 15078916]

27. Mulders SM, et al. Water channel properties of major intrinsic protein of lens. J Biol Chem. 1995; 270:9010–9016. [PubMed: 7536742]

28. Chandy G, Zampighi GA, Kreman M, Hall JE. Comparison of the water transporting properties of MIP and AQP1. J Membr Biol. 1997; 159:29–39. [PubMed: 9309208]

29. Harries WE, Akhavan D, Miercke LJ, Khademi S, Stroud RM. The channel architecture of aquaporin 0 at a 2.2-A resolution. Proc Natl Acad Sci U S A. 2004; 101:14045–14050. [PubMed: 15377788]

30. Gonen T, et al. Lipid-protein interactions in double-layered two-dimensional AQP0 crystals. Nature. 2005; 438:633–638. [PubMed: 16319884]

31. Bok D, Dockstader J, Horwitz J. Immunocytochemical localization of the lens main intrinsic polypeptide (MIP26) in communicating junctions. J Cell Biol. 1982; 92:213–220. [PubMed: 7035467]

32. Costello MJ, McIntosh TJ, Robertson JD. Distribution of gap junctions and square array junctions in the mammalian lens. Invest Ophthalmol Vis Sci. 1989; 30:975–989. [PubMed: 2722452]

33. Gonen T, Sliz P, Kistler J, Cheng Y, Walz T. Aquaporin-0 membrane junctions reveal the structure of a closed water pore. Nature. 2004; 429:193–197. [PubMed: 15141214]

34. Girsch SJ, Peracchia C. Calmodulin interacts with a C-terminus peptide from the lens membrane protein MIP26. Curr Eye Res. 1991; 10:839–849. [PubMed: 1790714]

35. Reichow SL, Gonen T. Noncanonical binding of calmodulin to aquaporin-0: implications for channel regulation. Structure. 2008; 16:1389–1398. [PubMed: 18786401]

36. Schumacher MA, Rivard AF, Bachinger HP, Adelman JP. Structure of the gating domain of a Ca2+-activated K+ channel complexed with Ca2+/calmodulin. Nature. 2001; 410:1120–1124. [PubMed: 11323678]

37. Van Petegem F, Chatelain FC, Minor DL Jr. Insights into voltage-gated calcium channel regulation from the structure of the CaV1.2 IQ domain-Ca2+/calmodulin complex. Nat Struct Mol Biol. 2005; 12:1108–1115. [PubMed: 16299511]

38. Mori MX, Vander Kooi CW, Leahy DJ, Yue DT. Crystal structure of the CaV2 IQ domain in complex with Ca2+/calmodulin: high-resolution mechanistic implications for channel regulation by Ca2+ Structure. 2008; 16:607–620. [PubMed: 18400181]

39. Sarhan MF, Tung CC, Van Petegem F, Ahern CA. Crystallographic basis for calcium regulation of sodium channels. Proc Natl Acad Sci U S A. 2012; 109:3558–3563. [PubMed: 22331908]

40. Samso M, Wagenknecht T. Apocalmodulin and Ca2+-calmodulin bind to neighboring locations on the ryanodine receptor. J Biol Chem. 2002; 277:1349–1353. [PubMed: 11694536]

41. Huang X, Fruen B, Farrington DT, Wagenknecht T, Liu Z. Calmodulin-binding locations on the skeletal and cardiac ryanodine receptors. J Biol Chem. 2012; 287:30328–30335. [PubMed: 22773841]

42. Frank J, et al. SPIDER and WEB: processing and visualization of images in 3D electron microscopy and related fields. J Struct Biol. 1996; 116:190–199. [PubMed: 8742743]

43. Grigorieff N. FREALIGN: high-resolution refinement of single particle structures. J Struct Biol. 2007; 157:117–125. [PubMed: 16828314]

44. Pettersen EF, et al. UCSF Chimera--a visualization system for exploratory research and analysis. J Comput Chem. 2004; 25:1605–1612. [PubMed: 15264254]

45. Yap KL, Yuan T, Mal TK, Vogel HJ, Ikura M. Structural basis for simultaneous binding of two carboxy-terminal peptides of plant glutamate decarboxylase to calmodulin. J Mol Biol. 2003; 328:193–204. [PubMed: 12684008]

46. Fallon JL, et al. Crystal structure of dimeric cardiac L-type calcium channel regulatory domains bridged by Ca2+* calmodulins. Proc Natl Acad Sci U S A. 2009; 106:5135–5140. [PubMed: 19279214]

47. Kim EY, et al. Multiple C-terminal tail Ca(2+)/CaMs regulate Ca(V)1.2 function but do not mediate channel dimerization. Embo J. 2010; 29:3924–3938. [PubMed: 20953164]

48. Smart OS, Neduvelil JG, Wang X, Wallace BA, Sansom MS. HOLE: a program for the analysis of the pore dimensions of ion channel structural models. J Mol Graph. 1996; 14:354–360. 376. [PubMed: 9195488]

49. Jensen MO, Mouritsen OG. Single-channel water permeabilities of Escherichia coli aquaporins AqpZ and GlpF. Biophys J. 2006; 90:2270–2284. [PubMed: 16399837]

50. Jensen MO, et al. Dynamic control of slow water transport by aquaporin 0: implications for hydration and junction stability in the eye lens. Proc Natl Acad Sci U S A. 2008; 105:14430–14435. [PubMed: 18787121]

51. Hashido M, Ikeguchi M, Kidera A. Comparative simulations of aquaporin family: AQP1, AQPZ, AQP0 and GlpF. FEBS Lett. 2005; 579:5549–5552. [PubMed: 16225876]

52. Yang B, Verkman AS. Water and glycerol permeabilities of aquaporins 1–5 and MIP determined quantitatively by expression of epitope-tagged constructs in Xenopus oocytes. J Biol Chem. 1997; 272:16140–16146. [PubMed: 9195910]

53. Yuan T, Vogel HJ. Calcium-calmodulin-induced dimerization of the carboxyl-terminal domain from petunia glutamate decarboxylase A novel calmodulin-peptide interaction motif. J Biol Chem. 1998; 273:30328–30335. [PubMed: 9804795]

54. Gut H, et al. A common structural basis for pH- and calmodulin-mediated regulation in plant glutamate decarboxylase. J Mol Biol. 2009; 392:334–351. [PubMed: 19580813]

55. Xia XM, et al. Mechanism of calcium gating in small-conductance calcium-activated potassium channels. Nature. 1998; 395:503–507. [PubMed: 9774106]

56. Schumacher MA, Crum M, Miller MC. Crystal structures of apocalmodulin and an apocalmodulin/SK potassium channel gating domain complex. Structure. 2004; 12:849–860. [PubMed: 15130477]

57. Wang C, Wang HG, Xie H, Pitt GS. Ca2+/CaM controls Ca2+-dependent inactivation of NMDA receptors by dimerizing the NR1 C termini. J Neurosci. 2008; 28:1865–1870. [PubMed: 18287503]

58. Shi LB, Skach WR, Verkman AS. Functional independence of monomeric CHIP28 water channels revealed by expression of wild-type mutant heterodimers. J Biol Chem. 1994; 269:10417–10422. [PubMed: 7511600]

Methods-only references

59. Mindell JA, Grigorieff N. Accurate determination of local defocus and specimen tilt in electron microscopy. J Struct Biol. 2003; 142:334–347. [PubMed: 12781660]

60. Emsley P, Cowtan K. Coot: model-building tools for molecular graphics. Acta Crystallogr D Biol Crystallogr. 2004; 60:2126–2132. [PubMed: 15572765]

61. Phillips JC, et al. Scalable molecular dynamics with NAMD. J Comput Chem. 2005; 26:1781–1802. [PubMed: 16222654]

62. Mackerell AD, et al. All-Atom Empirical Potential for Molecular Modeling and Dynamics Studies of Proteins. J Phys Chem B. 1998; 102:3586–3616. [PubMed: 24889800]

63. Klauda JB, Brooks BR, MacKerell AD Jr, Venable RM, Pastor RW. An ab initio study on the torsional surface of alkanes and its effect on molecular simulations of alkanes and a DPPC bilayer. J Phys Chem B. 2005; 109:5300–5311. [PubMed: 16863197]

64. Jorgensen WL, Chandrasekhar J, Madura JD, Impey RW, Klein ML. Comparison of simple potential functions for simulating liquid water. The Journal of Chemical Physics. 1983; 79:926–935.

65. Essmann U, et al. A smooth particle mesh Ewald method. The Journal of chemical physics. 1995; 103:8577–8593.

66. Grubmuller H, Heller H, Windermuth A, Schulten K. Generalized Verlet Algorithm for Efficient Molecular Dynamics Simulations with Long-range Interactions. Molecular Simulations. 1991; 6:121–142.

67. Martyna GJ, Tobiax DJ, Klein ML. Constant pressure molecular dynamics algorithms. The Journal of Chemical Physics. 1994; 101:4177–4189.

68. Feller SE, Zhang Y, Pastor RW, Brooks BR. Constant pressure molecular dynamics simulation: The Langevin piston method. The Journal of chemical physics. 1995; 103:4613–4621.

69. Humphrey W, Dalke A, Schulten K. VMD: visual molecular dynamics. J Mol Graph. 1996; 14:33–38. 27–38. [PubMed: 8744570]
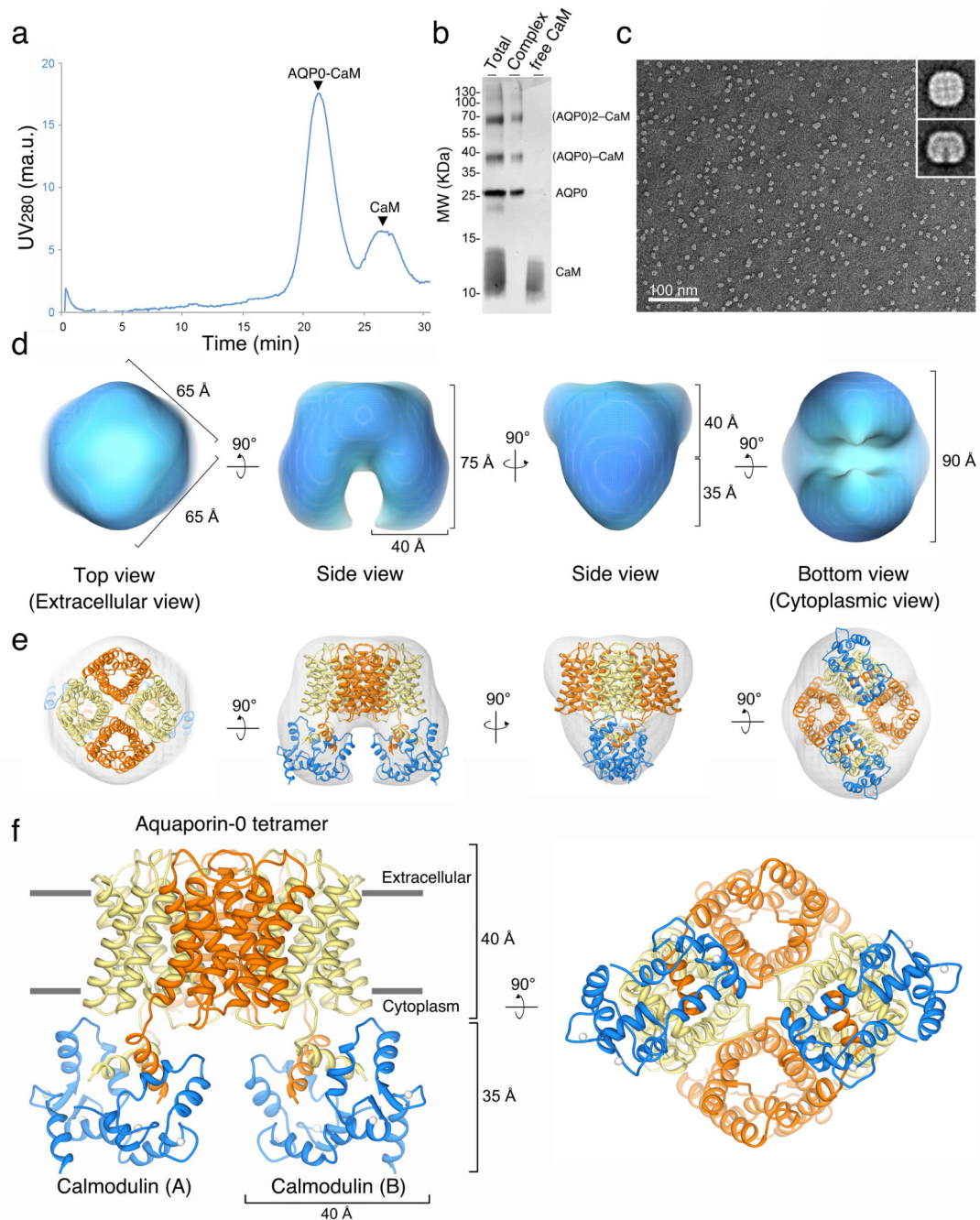
Figure 1. Purification and pseudo-atomic model of the aquaporin-0 – calmodulin complex (AQP0–CaM) determined by electron microscopy

(**a**) Chromatogram showing purification of the AQP0–CaM cross-linked complex from excess free calmodulin (CaM) by size-exclusion chromatography (SEC). (**b**) Silver stained SDS-PAGE showing fractions from the SEC purification. *Lane 1* shows the total starting material. *Lane 2*, the purified AQP0–CaM cross-linked complex dissociated into three protein bands in SDS migrating at 26kD, 39kD and 65kD. These bands correspond to the AQP0 monomer, the 1:1 AQP0–CaM cross-link and the 2:1 (AQP0)₂–CaM cross-link,

respectively. *Lane 3*, is the free CaM migrating as a diffuse band ~13kD. The fully assembled AQP0–CaM complex (*Lane 2*) dissociates to the 2:1 AQP0–CaM complex, the 1:1 AQP0–CaM complex, and the AQP0 monomer under denaturing SDS conditions due to the stochastic occurrence of peptide bonds made during the cross-linking reaction. (**c**) Electron micrograph of negatively stained AQP0–CaM particles. *Inset*, contains symmetrized projection averages of the AQP0–CaM complex (**d**) Different "views" of the three-dimensional (3D) reconstruction of the AQP0–CaM complex. (**e**) Fitting of the crystallographic structures of AQP0 (orange and yellow) and CaM (blue) into the 3D reconstruction (grey mesh). (**f**) Pseudo-atomic model of the AQP0–CaM complex displaying two CaM molecules (A and B) bound to the cytoplasmic C-terminal helices of the AQP0 tetramer.
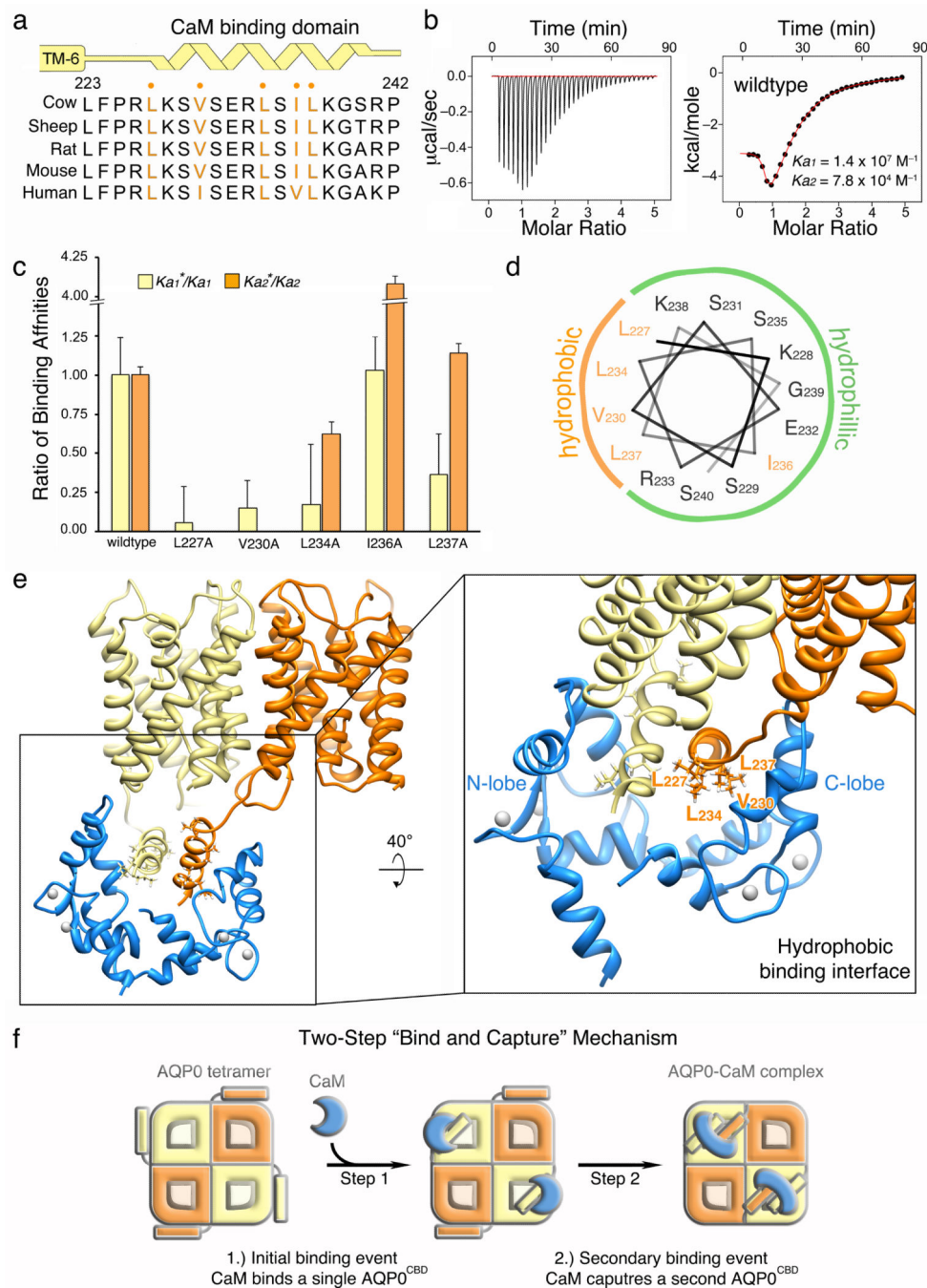
Figure 2. Hydrophobic interactions involved in AQP0–CaM complex formation
(**a**) Schematic of the secondary structure (yellow) and primary sequence alignment (blue) of the AQP0 calmodulin binding domain (AQP0^{CBD}). Residues in orange indicate conserved hydrophobic residues within the α-helical AQP0^{CBD}. (**b**) (*left*) ITC raw heats of binding Ca^{2+}–CaM to the wildtype AQP0^{CBD} peptide and (*right*) binding isotherm fit with a two-state binding model. (**c**) Ratio of binding affinities obtained by ITC for AQP0^{CBD} peptides when each hydrophobic site (• in panel A) was mutated to alanine. (**d**) Helical wheel analysis identifies a hydrophobic face involved in CaM recognition. (**e**) Structure of AQP0–
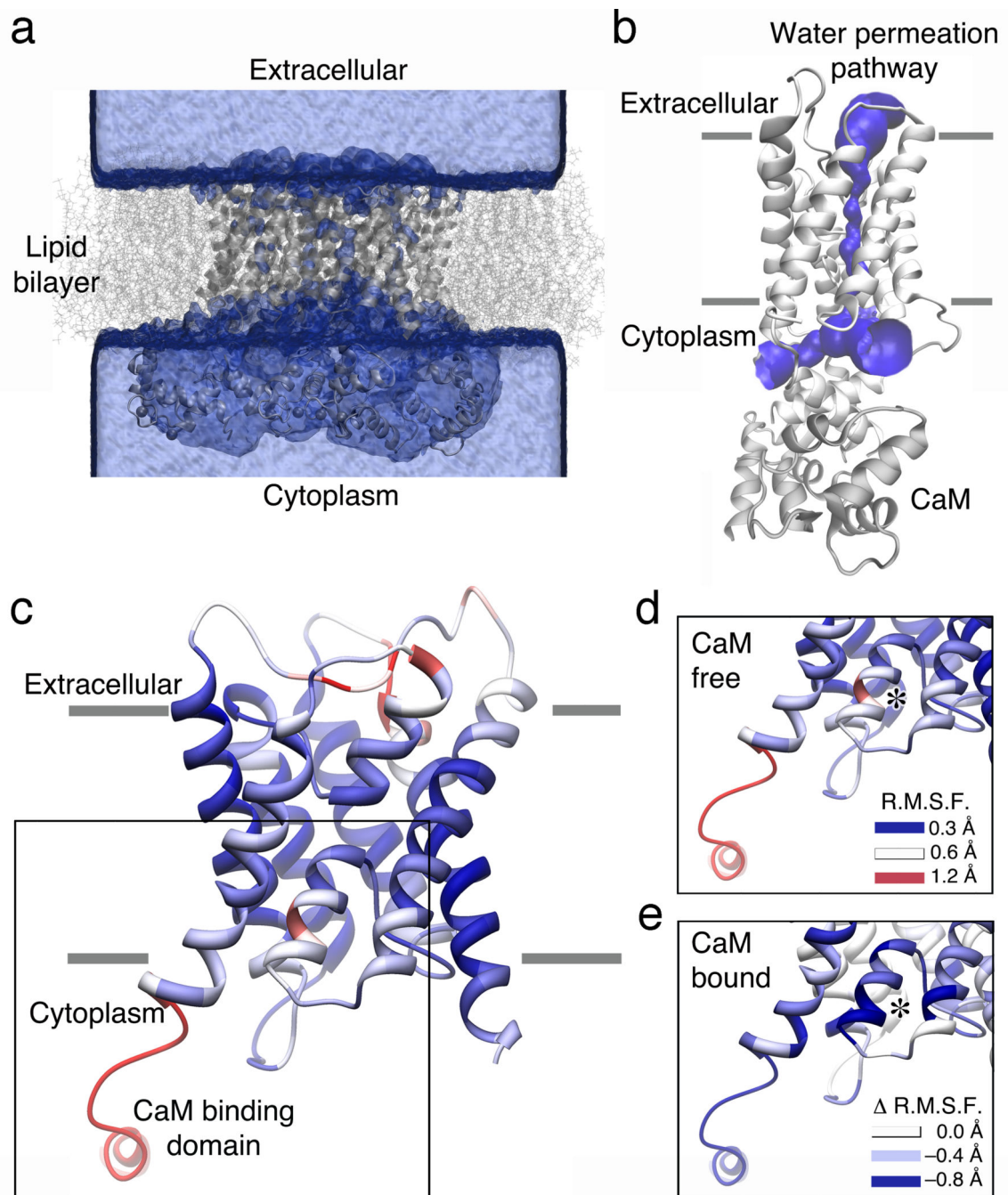
CaM showing two AQP0 monomers bound to CaM (colored as in Figure 1). *Zoom-view*, shows the AQP0^{CBD} (yellow and orange helices) with AQP0 residues forming the proposed hydrophobic interface with CaM shown as stick representations. **(f)** Schematic illustrating the two-step "bind and capture" mechanism for assembling the 2:1 AQP0–CaM complex, described in the main text.

Figure 3. Calmodulin restricts the dynamics of AQP0

(**a**) Water density (blue iso-surface) for the equilibrated AQP0–CaM (grey ribbon) in a lipid bilayer (grey stick). (**b**) Pore profile analysis using the program HOLE[48] showing water permeation pathway (blue surface) in the CaM-bound conformation of the AQP0 protomer (white and grey ribbon). (**c**) CaM-free per-residue root-mean-square fluctuation (RMSF) values mapped to the AQP0 structure according to color (RMSF = 0.3 Å – blue, 0.6 Å – white and 1.2 Å – red). (**d**) Zoom view of the cytoplasmic domain of AQP0. (**e**) Change in protein dynamics (RMSF) of the CaM-bound system compared to the CaM-free system
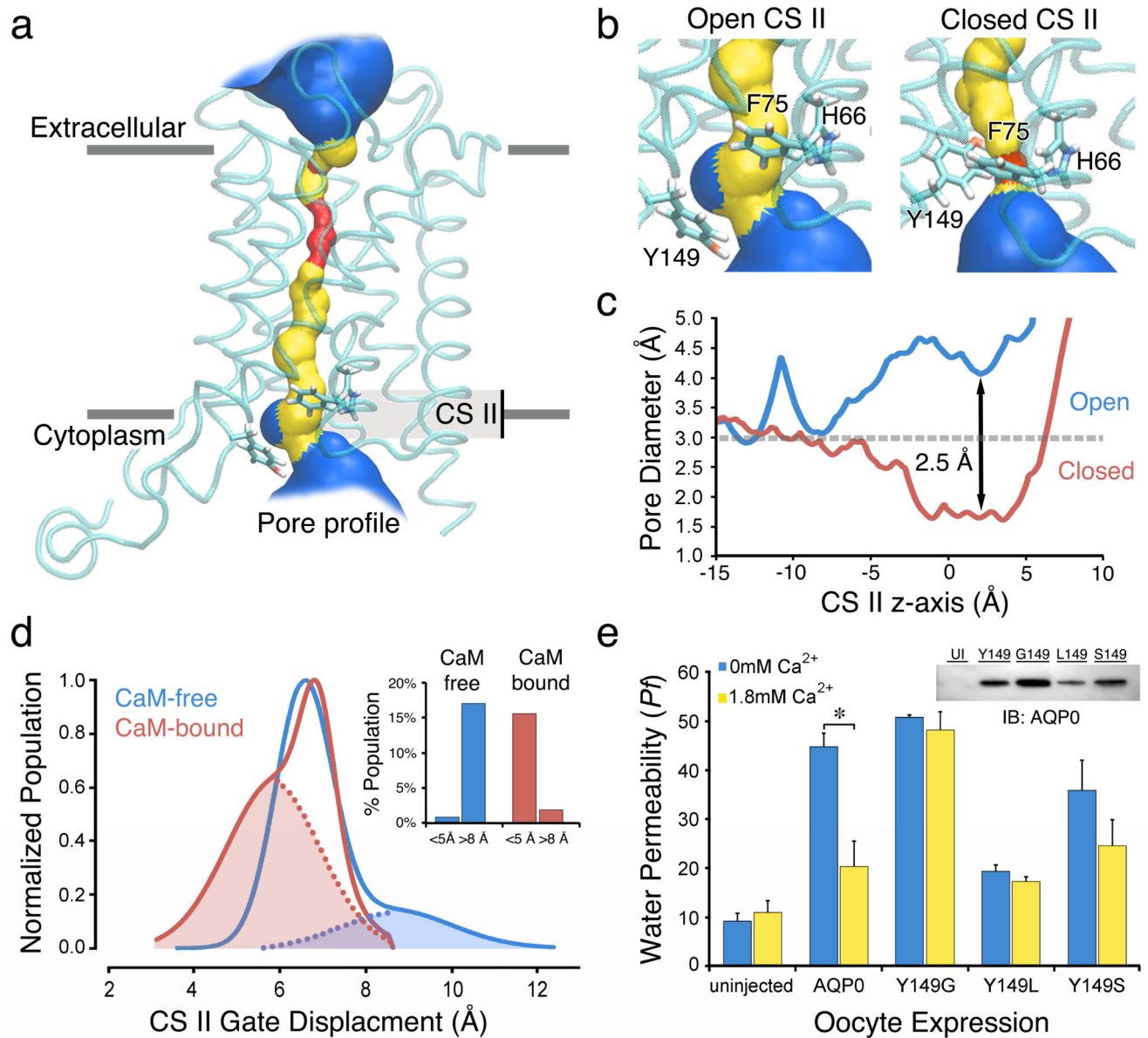
mapped to the AQP0 structure according to color (RMSF. = 0 Å – white, −0.4 Å – light blue, −0.8 Å – dark blue). Asterisks in (**d** and **e**) indicate the position of the AQP0 cytoplasmic constriction site II (CSII).

Figure 4. CaM binding closes the AQP0 cytoplasmic constriction site gate II (CSII)
(**a–c**) Pore profile analysis of AQP0 during the molecular dynamics (MD) simulation. The location of CSII is indicated in (**a**). Side chains of the CSII residues Tyr149, Phe75 and His66 are displayed as sticks. (**a** and **b**, *left panel*) Tyr149 in a downward "open" conformation. (**b**, *right panel*) Tyr149 in an upward "closed" conformation. (**c**) Plot indicating the pore diameter of the open AQP0 CSII (green) and the closed CSII (red). (**d**) Plot indicating the population of structures obtained during the CaM–free AQP0 (green) and CaM–bound AQP0 (red) MD simulations clustered according to the displacement of their CSII residues Tyr149 and Phe75. (**d**, *inset*) Plot showing the population of structures with CSII displacement < 5 Å and > 8Å. (**e**) Water channel permeability rates (P_f, um•s^{-1}) obtained from Oocytes expressing wildtype AQP0 and CSII mutants (Y149G, Y149L, Y149S) obtained under 0mM (blue) and 1.8 mM Ca^{2+} (green) buffer conditions. The AQP0

P_f is significantly inhibited by Ca^{2+} ($P = 0.012$). This effect has previously been shown to be CaM dependent[14]. The water permeability rates of CSII mutant AQP0 channels were deficient in Ca^{2+} regulation. Each construct was expressed and correctly trafficked to the plasma membrane as demonstrated by immune-blot analysis (**e**, *inset* and Supplementary Figure S5). Although expression levels varied among the mutants only WT AQP0 was acutely Ca^{2+} sensitive and mutation in Y149 generally abolished Ca^{2+} sensitivity.
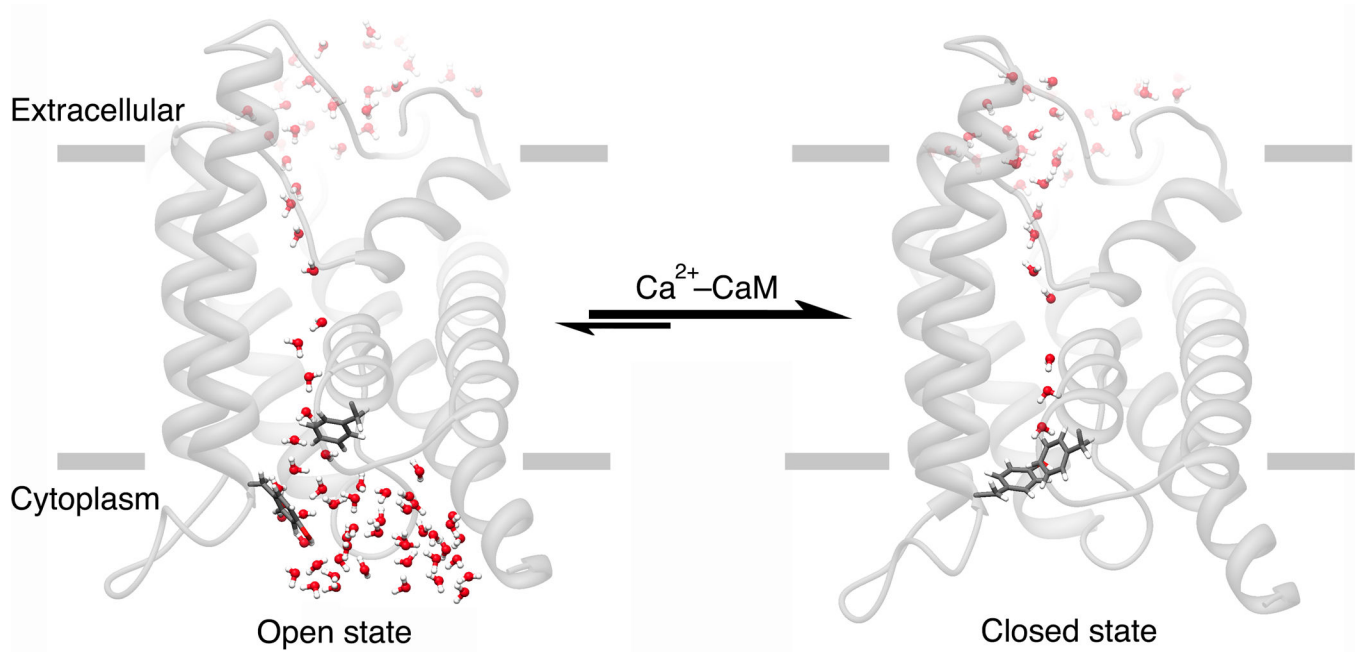
Figure 5. Mechanism of Ca^{2+}–CaM regulation of AQP0

The AQP0 water channel exists in equilibrium between an open state (*left*) and closed state (*right*). These states are formed by dynamic conformational changes at the cytoplasmic constriction site (CSII) formed by residues Tyr149, Phe75 and His66. Binding of Ca^{2+}–CaM at the C-terminus of AQP0 results in a shift in this equilibrium by allosterically stabilizing the closed CSII state, thereby restricting water channel permeability. The structural models were obtained from the MD simulations. AQP0 is shown as grey ribbon and water molecules in red. Some water molecules were deleted in the figure for display purposes and clarity only. Likewise, The last transmembrane helix of AQP0 is removed for clarity. CSII residues Tyr149 and Phe75 are shown as stick representations.